Open Ceramics 16 (2023) 100442

Contents lists available at ScienceDirect

Open Ceramics

journal homepage: www.sciencedirect.com/journal/open-ceramics

Comparison of conventional crushing and high-voltage pulsed power technology as techniques for disaggregating different types of spent magnesia-carbon refractory bricks during recycling

Andrie Garbers-Craig [a,*], Natasia Naude [b]

[a] Centre for Pyrometallurgy, Department of Materials Science and Metallurgical Engineering, University of Pretoria, South Africa
[b] Minerals Processing Group, Department of Materials Science and Metallurgical Engineering, University of Pretoria, South Africa

ARTICLE INFO

Handling Editor: Dr P Colombo

Keywords:
MgO-C bricks
Conventional crushing
HVPPT

ABSTRACT

Three different types of spent magnesia-carbon (MgO–C) bricks were chosen to evaluate the liberation of magnesia particles through high-voltage pulsed power technology (HVPPT) and conventional comminution (jaw and cone crushing). The primary objective was to determine how the different types of MgO–C bricks comminute and whether magnesia particles could be restored to their original raw material particle size distribution (PSD).

Analytical results revealed that the bricks contained varying amounts of graphite and resin binder, indicating differences in their compositions and therefore comminution properties. The HVPP technique demonstrated its ability to liberate magnesia particles within the +1700 μm fraction, whereas conventional crushing predominantly formed composite particles (containing MgO and carbon) within this size range, with over 63% particles falling in this category. This finding suggests that MgO particles were not adequately liberated during the conventional crushing process, indicating the need for an additional comminution step to achieve the desired liberation.

1. Introduction

The circular economy seeks to redefine how resources are used by promoting the circulation of materials to optimise resource efficiency, minimise environmental impacts, minimise waste and grow the workforce through job creation [1]. In the refractories industry a circular economy implies that refractories must be repaired where possible, while spent refractories must be reused and recycled to produce new refractory materials [2,3]. High energy requirements during refractory production (e.g. firing of formed products), CO_2 emission concerns as well as the increased cost of disposal and landfilling of spent refractories have increased interest in the recycling of refractory materials [4–6]. Closed-loop recycling, wherein a product is used, recycled and subsequently transformed into a new product, implies the preservation of natural resources through reduced consumption. Additionally, the lifespan of materials is extended, leading to the attainment of a more sustainable refractories industry.

Magnesia is one of the most important refractory raw materials as it is widely used in the steel, cement, glass, ferroalloy and non-ferrous industries [7]. It accounts for 25 and 30% of the total refractory mineral demand [8]. Since MgO–C bricks are widely used in basic oxygen (BOF) and electric arc furnaces (EAF) as well as ladles in the steel industry, it is sensible to recover magnesia from spent MgO–C bricks. Recycling magnesia from MgO–C bricks is complicated by the fact that these bricks are composite materials that consist of combinations of sintered and fused MgO grains (the main component), embedded in a matrix consisting of graphite or nano-sized carbon (sources such as nano carbon black, carbon nano tubes and expanded graphite), a carbonaceous binder (such as phenolic resin) and anti-oxidants [9–11]. Anti-oxidants (which protect the carbon from oxidation) can be in the form of metals (e.g. Al, Si, Mg), alloys (e.g. Al–Mg and Al–Si), carbides (e.g. B_4C, SiC, $Al_4Si_2C_5$, Al_4O_4C) and borides (e.g. ZrB_2, MgB_2, LaB_6) [12]. Conventional MgO–C bricks contain 12-18 mass% graphite, while the low-carbon MgO–C bricks contain nano-carbon in combination with low amounts of graphite (1–5 mass%) [12–14]. Adding large amounts of carbon to a MgO–C brick leads to higher heat losses and higher shell temperatures, as well as increased carbon pick-up into the steel [13]. These limitations have led to the development of low-carbon MgO–C bricks in which other carbon sources are used. Nano-carbon can reduce the carbon contents in these bricks without sacrificing the benefits of

* Corresponding author.
E-mail address: andrie.garbers-craig@up.ac.za (A. Garbers-Craig).

https://doi.org/10.1016/j.oceram.2023.100442
Received 5 June 2023; Received in revised form 21 August 2023; Accepted 22 August 2023
Available online 25 August 2023

Fig. 1. Heap of discard oxide-carbon bricks at Philmar Consulting.

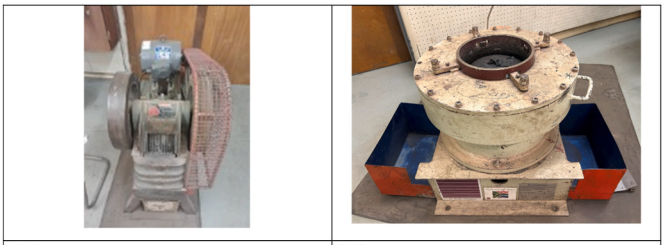

Fig. 2. Denver jaw crusher (a) and Osborn cone crusher (b) used in this study.

carbon addition [13]. Bag and co-workers [15] reported that a mixture of 0.9% amorphous carbon black with 3 mass% graphite could result in a MgO–C brick of quality similar to 10–18% carbon bricks.

Spent MgO–C bricks have over the years been recycled in a number of ways, namely as slag conditioner in order to achieve MgO saturation and effectively foam EAF slags [16–18], as a secondary raw material for MgO–C brick production [19–21] or as secondary MgO raw material from which carbon has been removed through calcination [22]. Fines from spent MgO–C bricks have also been used as a reactive medium for removal of Co and Ni from contaminated groundwater [23], while portions of unaffected MgO–C have been reused as a pre-wall in front of new lining bricks in the EAF [24]. When crushing spent MgO–C bricks for recycling as a slag conditioner to the EAF, Bennet et al. [25] suggested that the particle size after crushing should be less than 3 mm to achieve complete dissolution in the slag.

Investigations have also started on methods whereby MgO–C bricks can be recycled through the liberation and separation of MgO and graphite aggregate grains, from which pure raw materials can be recovered. Struble et al. however, reported that this can only be achieved at particle sizes of −45μm [26]. Different comminution methods

Fig. 3. SelFrag Lab S2.1 unit (a) and processing vessel with pieces of MgO–C brick (b).

Table 1
ICP-OES and LECO C analyses of the selected discard bricks (mass%).

	Brick I	Brick II	Brick III
MgO	76.84	81.20	91.05
Al_2O_3	0.47	0.33	0.47
SiO_2	3.03	0.79	1.12
CaO	1.26	1.76	2.07
FeO	0.29	0.28	0.30
C (Graphite)	13.2	13.0	0.1
C (Organic)	4.83	1.90	4.38

are therefore being investigated, with the aim of liberating the valuable material at its coarsest possible size [27]. This process requires the careful selection of crushers and other equipment to achieve desired results with minimal energy consumption. Jaw crushers are typically used as primary crushers due to their low operating costs and simple maintenance requirements. Secondary cone crushers can be utilized to obtain the desired size distribution and liberation. Additionally, various types of crushers are available on the market that can accommodate different hardness levels and capacities, depending on the application requirements [28–30]. Therefore, it is important to select the appropriate crusher which will provide efficient operation with a minimum energy expenditure for the comminution processes to be successful.

HVPPT is a relatively new development in comminution [31]. It is an electric-dynamic crushing technique, during which discharge channels for the current form inside the sample being crushed [32,33]. Because of the differences in electrical properties among various minerals or materials in the sample, these discharge channels generate tension along the interfaces of these minerals or materials, resulting in breakage. High-voltage pulsed power technology has been widely studied in the mineral processing industry for enhancing the liberation of minerals in ores and coal, metals in slags, as well as metal fibres in fibre-reinforced concrete [34–37]. This technology has also found applications in pre-weakening and pre-concentration of ores [31], electronic waste recycling [38] and the recycling of PV panels [39].

This paper focuses on determining the comminution behaviour of various types of spent MgO–C refractory bricks. The objective was to explore the potential of liberating the magnesia grains from these bricks to their original size using HVPPT and to compare this technique with a two-stage comminution process involving a jaw crusher and cone crusher.

2. Experimental

2.1. Materials and sample preparation

Bricks were randomly sampled from a heap of discard oxide-carbon bricks at Philmar Consulting, Olifantsfontein, South Africa (Fig. 1). The supplier(s) of these bricks and the environment in which they were used, are not known. These bricks were sorted with a hand-held X-ray fluorescence (XRF) analyzer [40], after which three different types of MgO–C bricks were selected for the comminution test work. From each brick, three sub-samples were cut: one sub-sample for chemical and

Table 2
Quantitative XRD analysis of the spent bricks (mass%).

Sample	Brick I	Brick II	Brick III
Periclase	91.1	88.0	91.3
Forsterite	0.1	0.0	4.6
Monticellite	0.7	0.8	3.2
Merwinite	0.0	0.0	0.2
Spinel	0.6	2.3	0.1
Al	0.9	0.1	0.0
Graphite-2H	6.7	8.8	0.6
Total	100.0	100.0	100.0

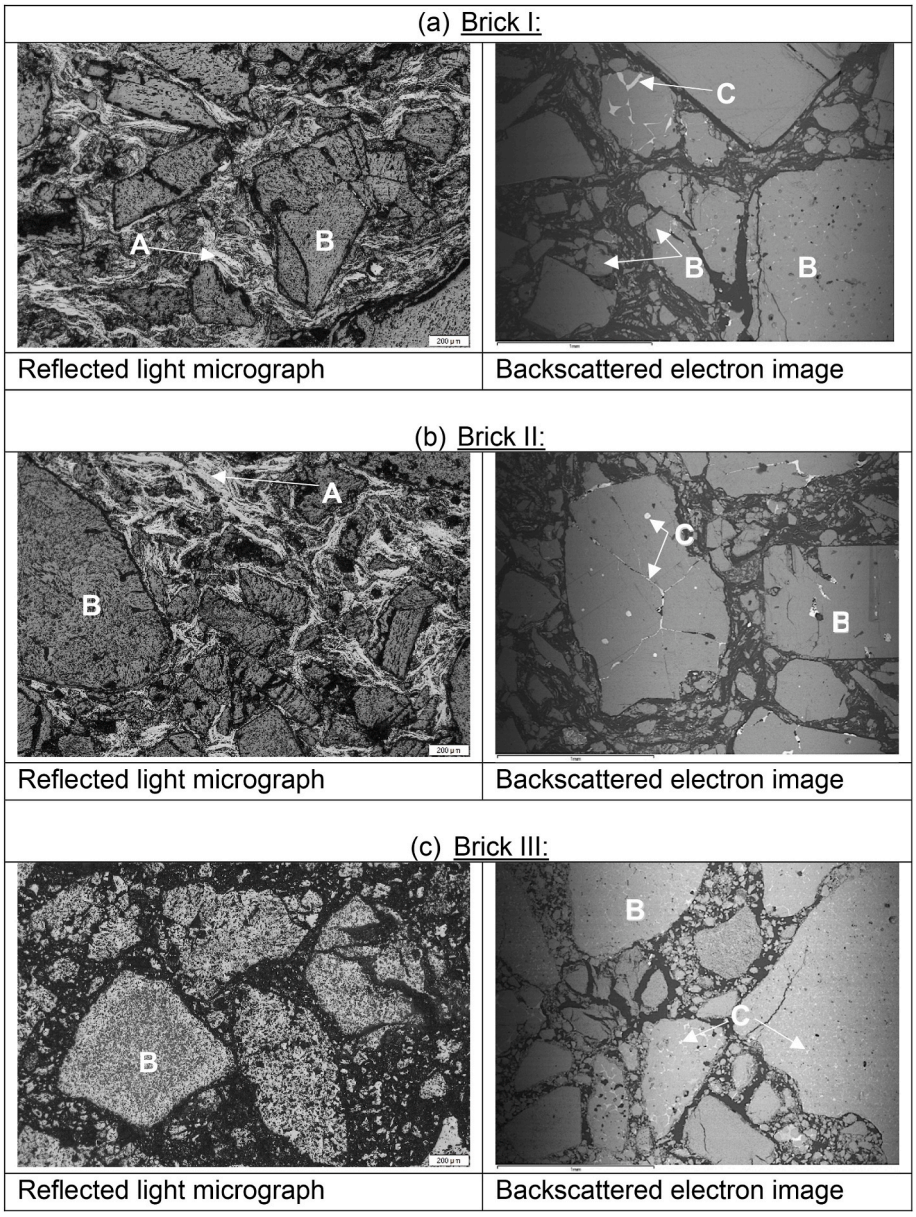

Fig. 4. Microstructures of discard Brick I (a), Brick II (b) and Brick III (c) (A = graphite; B=MgO; C = silicate impurity phase).

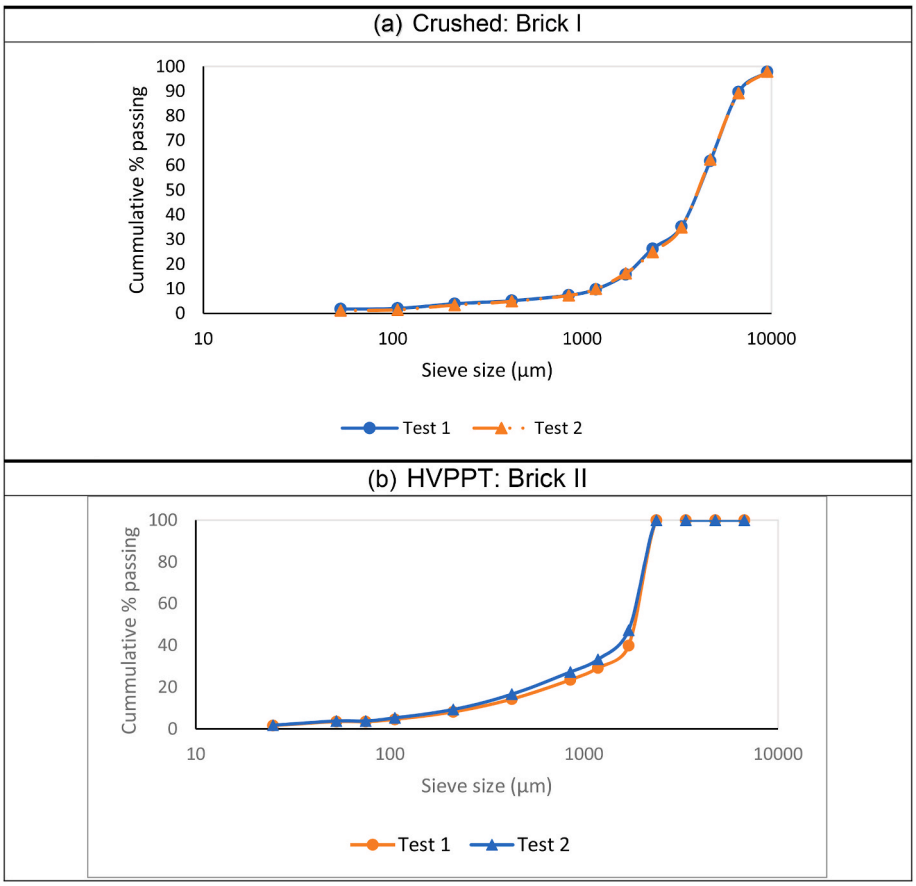

Fig. 5. Repeatability of PSD analyses when using conventional crushing (a) and HVPPT (b).

phase chemical analysis, one sub-sample for conventional crushing tests (jaw and cone crushing), and one sub-sample for the HVPP test work. The samples were ground and micronized for chemical and X-ray diffraction (XRD) analyses, while polished sections were prepared for reflected light microscopy, scanning electron microscopy - energy dispersive spectrometry (SEM-EDS) and image analysis. Stereo and reflected light microscopy were used for microstructure analysis. SEM-EDS analysis was used for both microstructure and phase compositional analyses.

2.2. Comminution techniques used

The spent MgO–C refractory bricks were cut into equal sized samples. These samples were further reduced in size according to the required testing methodology, after which they were exposed to conventional crushing or HVPPT.

2.2.1. Conventional crushing

A two-stage crushing methodology was needed to compare with the HVPPT. A Denver (Fig. 2) laboratory jaw crusher (closed side setting (CSS) = 20 mm) was used as the primary crusher and an Osborn laboratory cone crusher (CSS = 3 mm) was used as the secondary crusher.

Samples designated for conventional crushing were initially processed by the primary jaw crusher. The output from the jaw crusher was subsequently fed into the secondary cone crusher, after which the particle size distribution (PSD) of the sample was determined through wet sieving. To ensure that representative samples were taken for microstructure analysis, the samples were split into the appropriate sample mass as required for each specific analytical technique, using a 10-way Dickie and Stockler rotary splitter in accordance with ISO 3082:2017 regulations.

2.2.2. HVPPT

HVPP comminution was performed using a SelFrag Lab S2.1 unit at the Geology Department, University of Pretoria, South Africa (Fig. 3a). The MgO–C brick samples allocated for HVPPT tests were cut into smaller pieces with dimensions of 10 mm × 20 mm x 40 mm to fit the processing vessel of the SelFrag unit (Fig. 3b). These pieces were combined whereby sample sizes of between 470 and 150g were used per experiment. Water was used as dielectric medium.

The process parameters that were varied included the gap between the electrodes (10–20 mm), voltage of the discharges (120–180 kV), pulse rate (1–5 Hz) as well as the number of pulses (4–250). Three series of experiments were performed: In the first series the repeatability of the crushing and HVPPT tests was evaluated, using Bricks I and II. In the second series the liberation of different raw materials in the different size fractions of the comminuted Brick III (conventional crushing vs. HVPPT) was evaluated, while in the third series the influence of energy input from the SelFrag unit on PSD was evaluated (Brick II). The generated energy of each HVPPT test was calculated using equation (1) and then converted to a specific energy ($kWht^{-1}$) [36]:

$$E = n\left[(0.5)\left(CU^2\right)\right] \quad (1)$$

Where E = total energy generated in joules (J); n = number of pulses; C = capacitance of the SelFrag unit in farad (F); U = pulse voltage (V).

After completion of each HVPPT test, the comminuted product was filtered, dried overnight at 110 °C, and the PSD determined through wet sieving. The various size fractions were again split in a rotary splitter, in order to obtain representative samples for phase and microstructure characterisation.

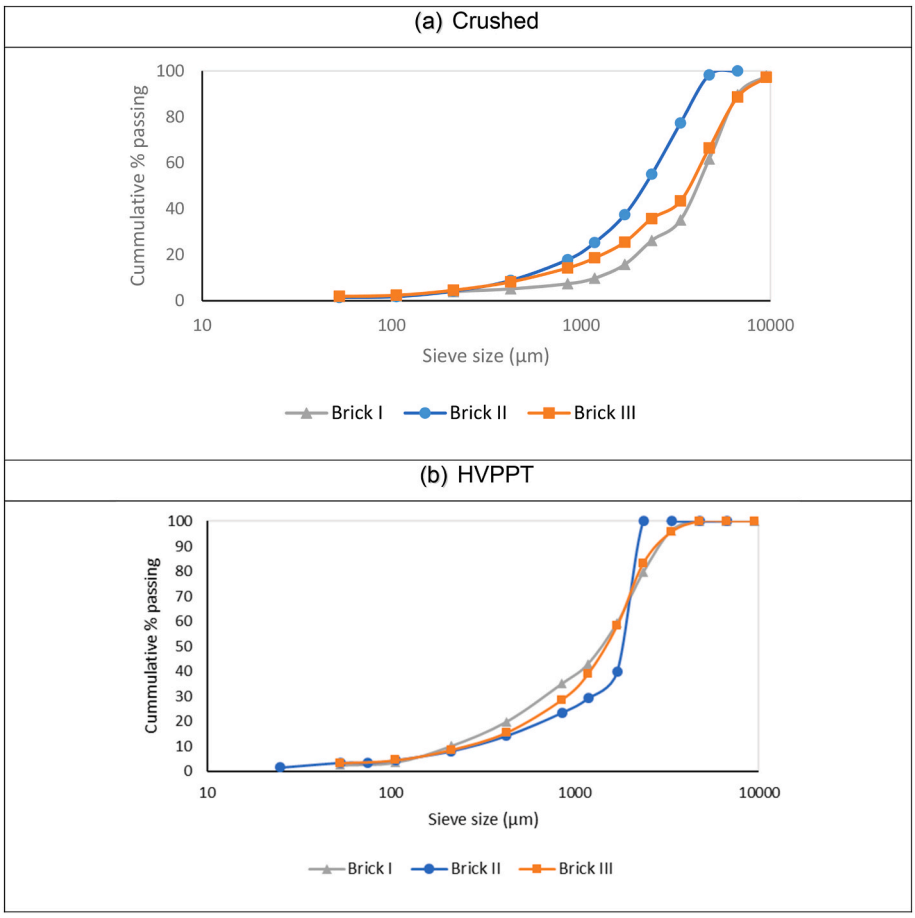

Fig. 6. PSD of 3 different bricks after crushing (a) and HVPPT (b).

2.3. Laboratory sieving

The PSDs of the crushed and HVPPT samples were determined through a wet laboratory sieve shaker test. This test adhered to the guidelines specified in ASTM D4749-87 (2012) [41]. During the test, each sample was subjected to shaking for a duration of 10 min at a frequency of 40 Hz to ensure reliable and representative results. The mass of the sample retained on each sieve size was dried and recorded.

2.4. Analysis techniques

Samples were characterised using ICP-OES (PerkinElmer 5300), LECO C, qualitative and quantitative XRD analysis (PANalytical X'Pert Pro powder diffractometer, Rietveld), stereo and reflected light microscopy as well as SEM-EDS analysis (Jeol JSM–IT300LV scanning electron microscope coupled with an Oxford X–Max 50 Energy–Dispersive X–ray Spectrometer).

The liberation of the MgO grains in Brick III was quantified through image analysis. Digital images were processed using Fiji, the open source image processing package based on ImageJ2.

3. Results and discussion

3.1. Spent bricks

3.1.1. Chemical and phase chemical compositions

ICP-OES and LECO C analysis indicated that Bricks I and II are high-carbon MgO–C bricks, which contain approximately 13 mass% graphite (Table 1). Brick III is a low-carbon MgO–C brick that contains virtually no crystalline graphite. It is assumed that the reported organic carbon in the bricks represents the carbonaceous binder, thereby indicating that Bricks I and II have similar binder contents.

The main impurity phase associated with the MgO raw materials used in all three bricks (as determined by XRD and EDS analyses) is monticellite ($CaMgSiO_4$). Trace amounts aluminium, spinel ($MgAl_2O_4$) and forsterite (Mg_2SiO_4) could be identified in Brick I, suggesting that a mixture of silicon and aluminium was added to this brick as antioxidants. It is assumed that during use these antioxidants oxidised to Al_2O_3 and SiO_2, which then reacted with the MgO fines (Table 2). Brick II also contains a noticeable amount of spinel. The forsterite and monticellite contents in Brick III are high. These silicate phases are associated with one of the two magnesia raw materials that were used in this brick. No carbides (Al_4C_3, SiC) or nitrides (AlN) could be detected in any of the three bricks.

3.1.2. Microstructures of the discard bricks

Reflected light micrographs and backscatter electron images (BEI) of the typical microstructures of Bricks I, II and III are shown in Fig. 4. From these images, it is evident that the microstructures of Bricks I and II are similar, while they differ from that of Brick III. The most significant difference is the presence of graphite flakes in the matrices of Bricks I and II, which cannot be detected in the matrix of Brick III. The presence of metallic particles (anti-oxidants) could not be detected by SEM analysis in any of the bricks. A high concentration of a silicate impurity phase along the grain boundaries of one of the MgO raw materials in Brick III was observed.

The maximum size of the MgO grains was found to be approximately 3 mm.

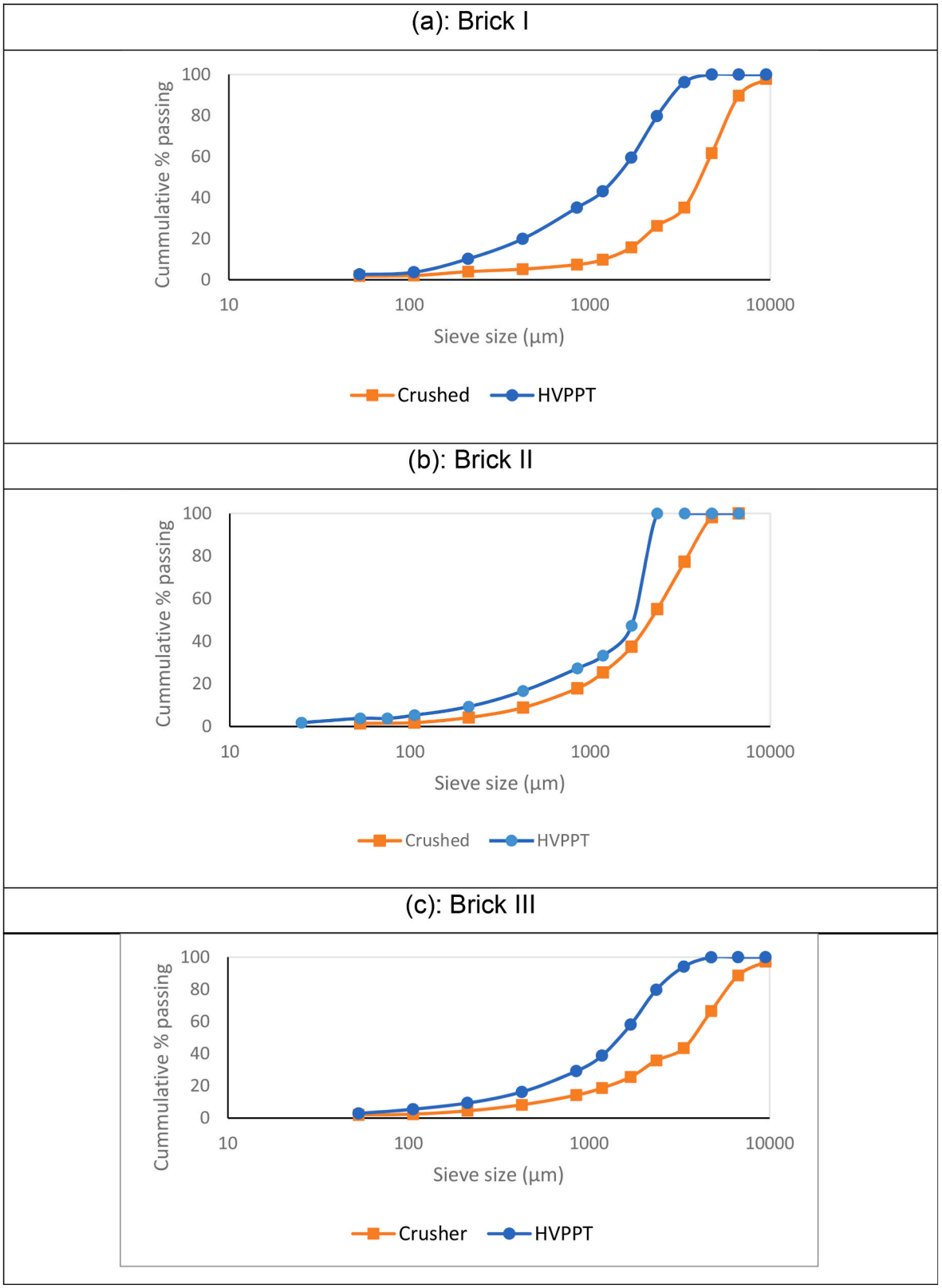

Fig. 7. Comparative PSD after crushing and HVPPT for Brick I (a), Brick II (b) and Brick III (c).

Table 3
$P_{80\%}$ and $D_{50\%}$ passing for the different bricks.

	Crushing (μm)		HVPPT (μm)	
	$P_{80\%}$	$D_{50\%}$	$P_{80\%}$	$D_{50\%}$
Brick I	5723	4210	2360	1400
Brick II	3350	2200	2000	1800
Brick III	6310	3810	2360	1500

Table 4
Mass percentage of +1700 μm fraction present.

	Crushing	HVPPT
Brick I	84.24	40.00
Brick II	62.55	60.11
Brick III	74.40	41.76

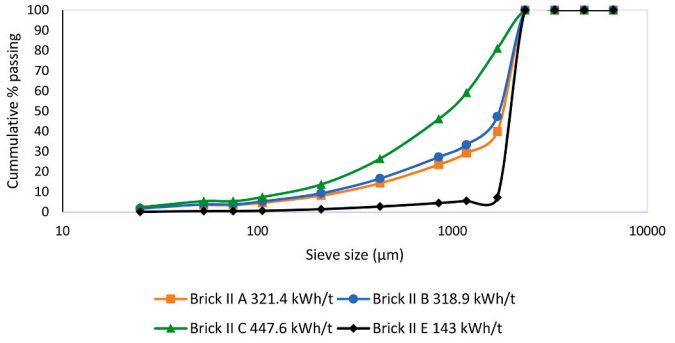

Fig. 8. Effect of energy input on Brick II.

3.2. Repeatability of crushing and HVPPT tests

Crushing and HVPPT responses were evaluated on Brick I and Brick II, as depicted in Fig. 5. Both processes yielded repeatable PSD results.

3.3. Particle size distributions of crushed vs. HVPPT samples

The PSD analyses of the different bricks after crushing and HVPPT are shown in Fig. 6. A comparison of the PSDs resulting from the two different techniques reveals that HVPPT generated significantly finer particles compared to the conventional two-stage crushing process involving a jaw crusher followed by a cone crusher. This highlights the need for an additional comminution step (milling) in the two-stage crushing circuit to achieve a similar PSD as that obtained with HVPPT [25].

When comparing the PSDs of the three crushed bricks (Fig. 6), a notable difference in the P80% (comminution efficiency) was observed between Brick II (3500 μm) versus Bricks I and III (5750 μm). Brick II exhibited a narrower size distribution, with a top size of −6700 μm, which is smaller than the 9500 μm observed for the other two bricks. This discrepancy suggests a significant difference in the way the three different MgO–C bricks break in the crusher, indicating that MgO–C bricks cannot be treated as a homogeneous group for crushing. The primary distinction between Bricks I and III versus Brick II lies in the lower organic carbon content (i.e. binder content) of the latter (Table 1).

The HVPPT results also indicated no substantial PSD difference between Brick I and Brick III. However, Brick II displayed an even narrower size distribution, presumably due to its low organic carbon content. The top size of Brick II (−2360 μm) was significantly lower than that of Bricks I and III (−4750 μm). Fig. 7 illustrates a comparison of the individual crushing and HVPPT results for each brick, revealing distinct differences in the PSD when using the HVPPT and conventional crushing techniques. The respective $P_{80\%}$ and $D_{50\%}$ (median) values for the

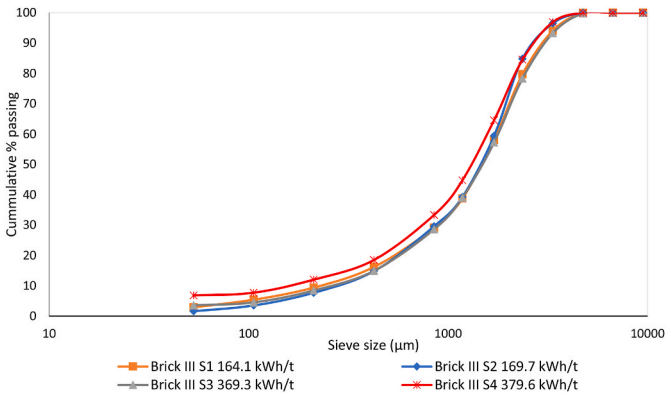

Fig. 9. Effect of energy input on Brick III.

different bricks are given in Table 3, demonstrating that the HVPPT material is considerably finer compared to the crushed material for each brick. The $D_{50\%}$ of Brick II indicates that a significant portion of the material falls within the size fraction 2360 μm–1700 μm.

The percentage of the +1700 μm fraction obtained after both the crushing and HVPPT processes is shown in Table 4. The selection of this size range was based on the observation that significant liberation was achieved for the HVPPT samples, whereas the crushing products still contained mostly composite particles, consisting of MgO and carbon. This implies that a substantial portion of the MgO in the HVPPT material will be liberated within this fraction. This is advantageous as it indicates that HVPPT requires only one comminution step to achieve liberation at the +1700 μm fraction, eliminating the need for additional comminution as required in the crushing process. Table 4 also indicates that the various types of MgO–C bricks cannot be treated as one commodity, but they need to be separated and comminuted differently.

3.4. Effect of energy input during the HVPPT tests

The energy input during the HVPPT tests was influenced by the imposed HVPPT conditions, as indicated in Fig. 8 for Brick II. Brick II C recorded the highest energy input (477.6 kWh/t), resulting in a sharp increase in the percentage of fines ($D_{50\%}$ = 950 μm). On the other hand, Brick II A and Brick II B had similar energy inputs (average = 320.15 kWh/t), yielding repeatable results of $D_{50\%}$ = 1750 and 1800 μm, respectively. Brick II E reflects the effect of a low energy input (143 kWh/t), resulting in minimal fines formation ($D_{50\%}$ = 2000 μm).

The effect of varying energy input is also illustrated for Brick III (Fig. 9). It can be concluded that only Brick III S4, with the highest energy input (379.6 kWh/t), exhibited a slight increase in the percentage of fines. The $D_{50\%}$ changed from 1500 μm (observed in all other bricks) to 1400 μm for Brick III S4. It is noteworthy to observe that the

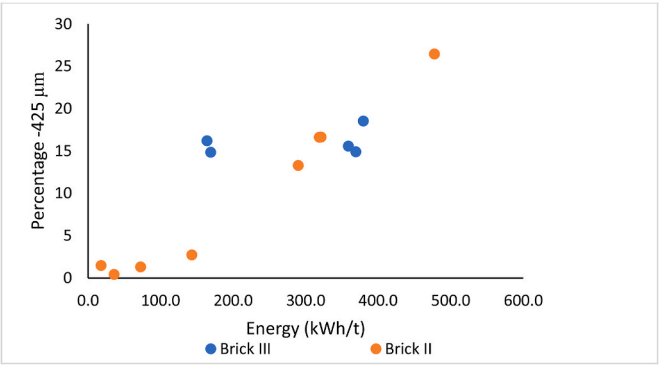

Fig. 10. Impact of energy input on the percentage −425 mm fraction.

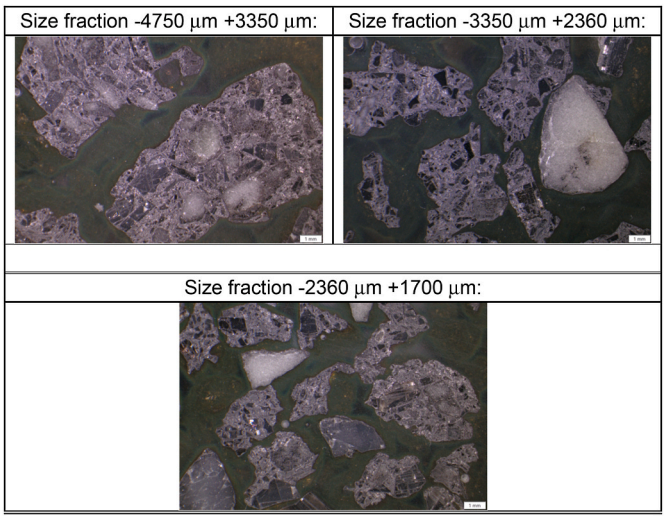

Fig. 11. Stereo micrographs of grains produced in the size range (−4750 µm + 1700 µm) when Brick I was crushed (white grains = MgO).

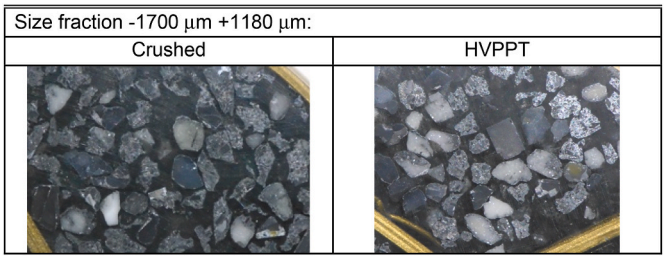

Fig. 12. Photographs of grains produced in the size range (−1700 µm + 1180 µm) when Brick II was crushed vs. comminuted by HVPPT (white grains = MgO).

PSD remained constant at all the different energy inputs (ranging from 164.1 to 369.3 kWh/t) for Brick III, but with a mere increase of 10.3 kWh/t, the PSD started to become finer.

Fig. 10 demonstrates the impact of energy input variation on the formation of particles sizes of −425 µm for Brick II and Brick III. The results indicate that less energy is required to crush Brick II compared to Brick III. Additionally, for Brick II, an increase in energy corresponds to a higher percentage of fines being produced.

3.5. Microstructures of grains produced during conventional crushing vs. HVPPT

After comminution (crushing and HVPPT), the resulting samples were dried and sieved. Samples were then taken from each size fraction for the preparation of polished sections for optical and SEM analyses. The microstructures of the particles that reported to the different size fractions from Bricks I and III are discussed in detail in sections 3.5.1 and 3.5.2. Since the microstructures of particles that formed from Brick II are similar to those of Brick I, only certain observations are highlighted for Brick II.

3.5.1. Bricks I and II

The (−4750 µm + 3350 µm) size fraction contained the largest grains that formed during conventional crushing of Brick I and Brick II, while with HVPPT comminution the largest grains fell in the (−1700 µm + 1180 µm) size fraction (Figs. 11 and 12). The grains in the crushed (−4750 µm + 3350 µm) size fraction consisted only of composite particles. These particles are constituted of MgO grains and graphite flakes, embedded in the carbonaceous binder. In the (−3350 µm + 2360 µm) crushed size fraction, and subsequent smaller size fractions, liberated MgO grains could be detected. Liberated MgO grains could be detected in all the HVPPT size fractions, of which the largest size fraction was (−1700 µm + 1180 µm). This implies that during the HVPP process some of the 3 mm MgO aggregate grains were broken down into smaller particles through intragranular fragmentation. The concentration of liberated MgO grains is higher in the HVPPT samples as compared to the conventionally crushed samples (Fig. 12). Characteristic of the MgO grains that were liberated during HVPPT comminution are their clean (unattached matrix constituents) and smooth rims.

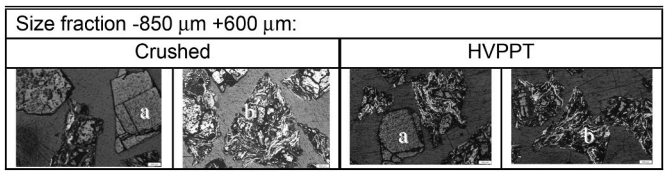

Fig. 13. Reflected light micrographs of the grains produced in the size range (−1700 µm + 600 µm) during comminution of Brick I
(a = liberated MgO grain; b = composite grain consisting of MgO grains, graphite flakes and carbonaceous binder).

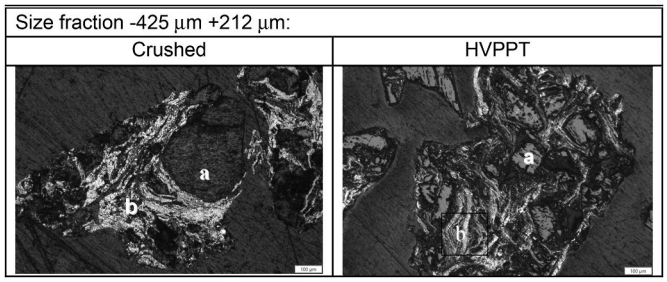

Fig. 14. Reflected light micrographs of the grains produced in the size range (−425 µm + 212 µm) during comminution of Brick II
(a = MgO; b = graphite).

The microstructure of the composite grains produced in the −1700 µm size fractions through crushing and HVPPT are similar (Fig. 13). These composite grains consist of medium size and fine MgO grains as well as graphite flakes that are embedded in a carbonaceous matrix, similar to the microstructure of the matrix portion of the brick. As the size fractions decrease in size, the degree of liberation of MgO grains increase. However, large portions of the MgO fines remain encapsulated, together with graphite flakes, in the composite particles (Fig. 14).

3.5.2. Brick III (S8)

Only composite particles were produced in the (−6700 µm + 2360 µm) size fraction of crushed Brick III, while liberated MgO grains were found in the (−4750 µm + 2360 µm) particle size range of HVPPT Brick III (S8) (Fig. 15). Characteristic of the MgO grains in this size fraction is their rounded edges as well as intragranular fragmentation of the large grains. Intragranular fragmentation occurred along the silicate impurity phase within the MgO grains, causing crystallites to become detached. At size distributions of −2360 µm the microstructures of the crushed vs. HVPPT particles started to look similar, with the only difference being the smoother rims of the liberated MgO grains in the HVPPT fractions (Figs. 15 and 16). In the size distribution range (−850 µm + 425 µm), the liberated MgO grains in the HVPPT sample exhibited some attachment of matrix material to their rims, although to a limited extent. However, all the particles looked similar in the −425 µm fractions, consisting of liberated MgO particles as well as composite particles (Fig. 16).

3.6. Liberation of MgO grains in brick III

The liberation of MgO grains during comminution was assessed not

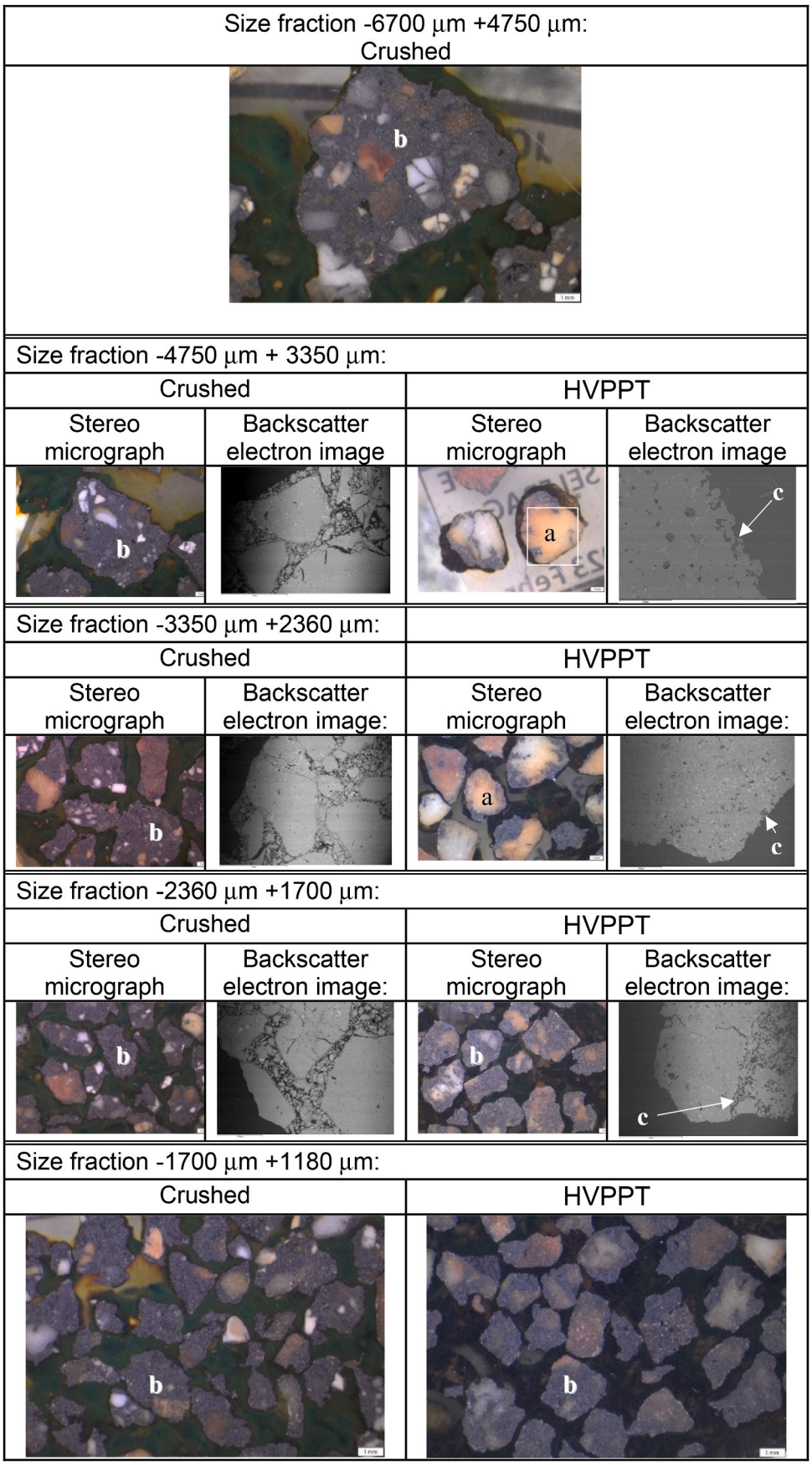

Fig. 15. Stereo micrographs of grains produced in the size range (−6700 μm + 1180 μm) during comminution of Brick III (a = MgO; b = composite particle; c = intragranular fragmentation along edge of large MgO grain).

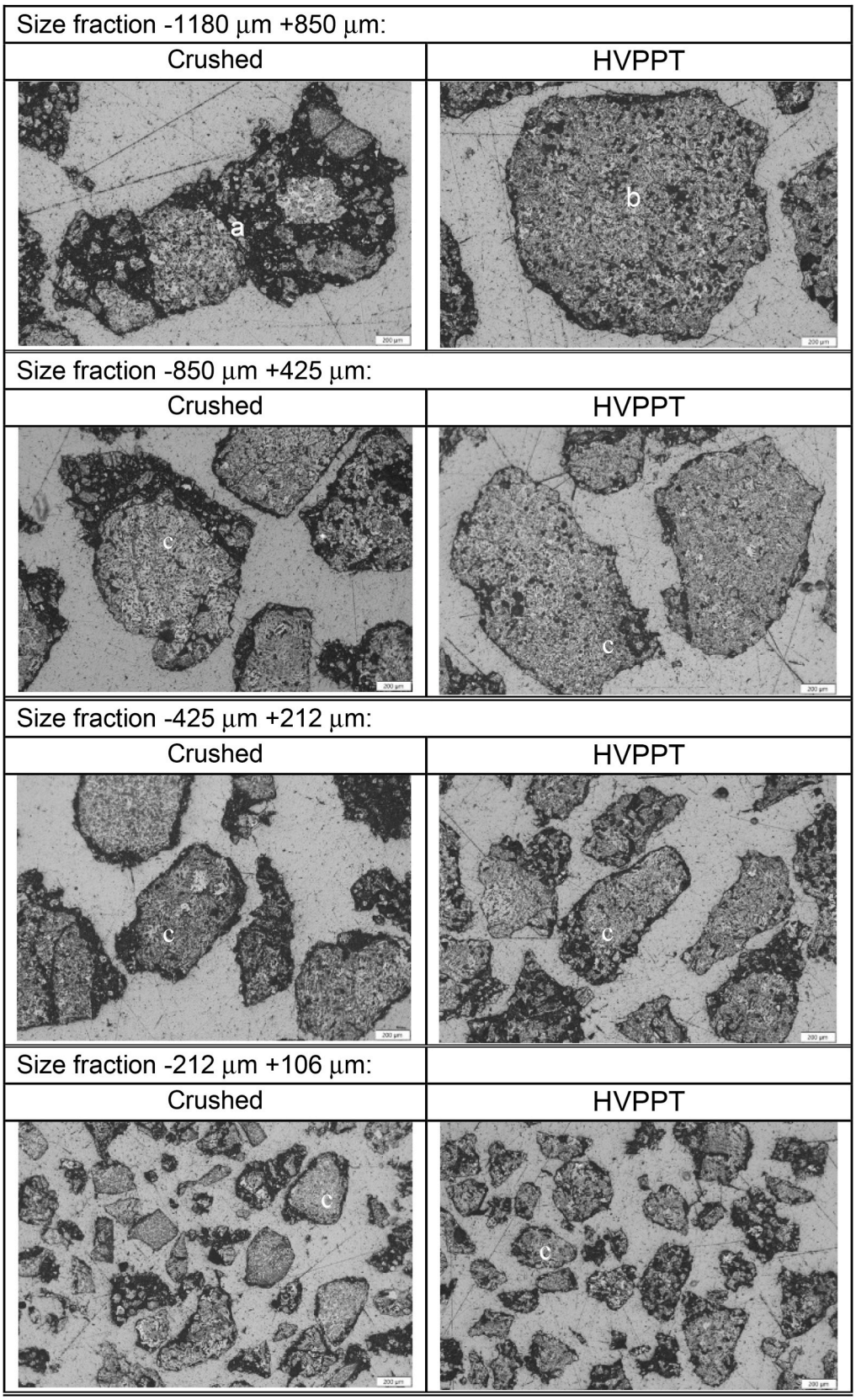

Fig. 16. Reflected light micrographs of the grains produced in the size range (−1180 µm + 106 µm) during comminution of Brick III (a = composite grain; b = liberated MgO grain; c = liberated MgO grain with thin layer of attached matrix material)
Fig. 16 (cont.). Reflected light micrographs of the composite grains produced in the size range (−106 µm + 53 µm) during comminution of Brick III.

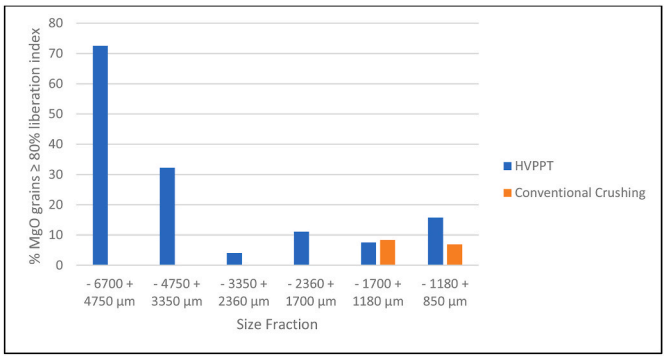

Fig. 17. Percentage of liberated MgO grains at an 80% liberation index in the different size fractions of Brick III.

only visually using optical microscopy and SEM analysis, but also quantified through image analysis by using photos of the different size fractions of crushed Brick III. Quantification was achieved by calculating the percentage of grains where MgO covered 80% or more of the total area. The liberation of MgO was significantly higher in the +1700 µm fractions produced by HVPPT as compared to conventional crushing (Fig. 17). This agrees with the observations obtained through optical microscopy and SEM analysis. When comparing the image analysis data of Fig. 17 with the PSD data in Tables 4 and it can be concluded that a significant portion (~42%) of the HVPPT-treated Brick III would be liberated, with virtually no liberation for 74% of the crushed Brick III.

4. Conclusions

In this study, conventional crushing was compared with HVPPT as a method of disaggregating different types of spent magnesia-carbon refractory bricks. The following conclusions can be drawn:

The microstructure of an MgO–C brick determines its crushing and fragmentation properties. The analytical results obtained from the three different MgO–C bricks revealed that Brick III had a low graphite content (0.1 mass%) compared to Brick I and Brick II (13 mass%). Additionally, Brick I and Brick III exhibited significantly higher levels of organic carbon (indicating a higher concentration of binder) compared to Brick II (4–5 mass% vs. 1.9 mass%). Brick II demonstrated a lower crushing strength in comparison to Brick I and Brick III and was more easily fragmented with an electric pulse, as confirmed by the results from both the crushing and HVPPT tests. Therefore, the comminution response of a brick is influenced by its organic carbon (binder) content.

Both HVPPT and conventional crushing yield repeatable PSD results. However, HVPPT consistently produces a finer product compared to the two stages of crushing, which is expected due to the breaking principles employed during HVPPT. To achieve similar results to HVPPT, the material obtained from the two stages of crushing would need a further comminution step.

HVPPT achieves a higher degree of liberation of MgO grains in the coarse fractions (+1700 µm), compared to conventional crushing.

Intragranular fragmentation occurred during HVPPT, leading to the release of crystallites from large aggregate grains and subsequent reduction in the size of the MgO grains. The extent of this breakage depends on the impurity content of the MgO raw material.

The percentage of particle breakage achieved through HVPPT is influenced by the energy input, but it is also influenced by the microstructure of the bricks themselves.

Funding

This research did not receive any specific grant from funding agencies in the public, commercial, or not-for-profit sectors.

Declaration of competing interest

The authors declare that they have no known competing financial interests or personal relationships that could have appeared to influence the work reported in this paper.

Acknowledgements

The authors gratefully acknowledge Philmar Consulting for providing the spent oxide-carbon bricks. Thanks are due to the following people from the University of Pretoria for their help in various aspects of this project: Dirk Odendaal (sample preparation), Mfesane Tshazi (crushing and screening), Jaco Delport and JP Nel (HVPPT), Awelani Moila and Prof Johan de Villiers (XRD analysis), as well as Wynand Roux (image analysis).

References

[1] W.R. Stahel, The circular economy, Nature (2016) 435–438, https://doi.org/10.1038/531435a.
[2] A. Spyridakos, D.E. Alexakis, I. Vryzidis, N. Tsotsolas, G. Varelidis, E. Kagiaras, Waste classification of spent refractory materials to achieve sustainable development goals exploiting multiple criteria decision aiding approach, Appl. Sci. 12 (2022) 3016, https://doi.org/10.3390/app12063016.
[3] H. Kunanz, B. Nonnen, J. Kirowitz, M. Schnalzger, Successful implementation of a high recycling containing magnesia-carbon brick in steel ladles, Bull. J. Refr. Innovations (2022) 17–20.
[4] L. Horckmans, P. Nielsen, P. Dierkx, A. Ducastel, Recycling of refractory bricks used in basic steelmaking: a review, Resour. Conserv. Recycl. 140 (2019) 297–304, https://doi.org/10.1016/j.resconrec.2018.09.025.
[5] L. McDonald, Fostering sustainability in the refractories industry, Am. Ceram. Soc. Bull. 101 (2022) 36–37.
[6] I. Muñoz, A. Soto, D. Maza, F. Bayón, Life Cycle Assessment of Refractory Waste Management in a Spanish Steel Works, vol. 111, Watse Manag., 2020, pp. 1–9, https://doi.org/10.1016/j.wasman.2020.05.023.
[7] The European Magnesite/Magnesia Industry: Enabler in the Transition to a Low-Carbon Economy, 2020 euromines_magnesite-decarbonisation_297x210mm_fin.pdf.
[8] IMFORMED, Imformed [Online], http://imformed.com/refractory-minerals-market-facing-up-to-the-future/, 2021.
[9] R. Kundu, R. Sarkar, MgO-C refractories: a detailed review of these irreplaceable refractroies in steelmaking, InterCeram Int. Ceram. Rev. 70 (2021) 46–54, https://doi.org/10.1007/s42411-021-0457-9.
[10] S. Mukherjee, S. Pramanik, S. Mukherjee, A comprehensive review of recent advances in magnesia carbon refractories, InterCeram Int. Ceram. Rev. 63 (2014) 90–98, https://doi.org/10.1007/BF03401039.
[11] S. Nanda, A. Choudhury, K.S. Chandra, D. Sarkar, Raw materials, microstructure, and properties of MgO-C refractories: directions for refractory recipe development, J. Eur. Ceram. Soc. 43 (2023) 14–36, https://doi.org/10.1016/j.jeurceramsoc.2022.09.032.
[12] Y. Cheng, T. Zhu, Y. Li, S. Sang, Microstructure and properties of MgO-C refractory with different carbon contents, Ceram. Int. 47 (2012) 2538–2546, https://doi.org/10.1016/j.ceramint.2020.09.099.
[13] S. Behera, R. Sirkar, Nano carbon containing low carbon magnesia carbon refractory: an overview, Protect. Met. Phys. Chem. Surface 52 (3) (2016) 467–474, https://doi.org/10.1134/S2070205116030059.
[14] M. Sathiyakumar, T. Mahata, S. Hazra, C. Delabaere, P.B. Panda, Low Carbon MgO-C Refractories for Clean Steel Making in Steel Ladles, METEC & 2nd ESTAD, 2015, pp. 1–7. Düsseldorf, 15-19 June 2015.
[15] M. Bag, S. Adak, R. Sarkar, Study on low carbon containing MgO-C refractory: use of nano carbon, Ceram. Int. 38 (2012) 2339–2346, https://doi.org/10.1016/j.ceramint.2011.10.086.
[16] F. Kek, T. Griessacher, C. Bauer, B. Zocratto, R. Krump, c. Koubek, Refractory waste to slag engineering solution – metallurgical consulting supports steel plant's circular economy strategy, Bull. J. Refr. Innovations (2022) 21–28.
[17] A.P. Luz, D.O. Vivaldini, F. López, P.O.R.C. Brant, V.C. Pandolfelli, Recycling MgO-C refractories and dolomite fines as slag foaming conditioners: experimental and thermodynamic evaluations, Ceram. Int. 39 (2013) 8079–8085.
[18] A.N. Conejo, R.G. Lule, F. Lopéz, R. Rodriguez, Reycling MgO-C refractory in electric arc furnaces, Resour. Conserv. Recycl. 49 (2006) 14–31, https://doi.org/10.1016/j.resconrec.2006.03.002.
[19] R. Kuriorowski, MgO-ZrO2 refractory ceramics based on recycled magnesia-carbon bricks, Construct. Build. Mater. 231 (2020), 117084, https://doi.org/10.1016/j.conbuildmat.2019.117084.
[20] M. Ludwig, E. Śnieżek, I. Jastrzębska, R. Prorok, M. Sulkowski, C. Golawski, C. Fischer, K. Wojteczko, J. Szczerba, Recycled magnesia-carbon aggregate as the component of new type of MgO-C refractories, Construct. Build. Mater. 272 (2021), 121912, https://doi.org/10.1016/j.conbuildmat.2020.121912.
[21] M. Ludwig, I. Jastrzębska, R. Prorok, M. Sulkowski, C. Golawski, J. Szczerba, Investigation of Recycled Magnesia-Carbon Aggregate Obtained with Omitting

Carbon Removal Step, UNITECR 2022, Downloaded from bulletin-archive.ceramics.Org.
[22] K. Moritz, N. Brachhold, J. Hubálkova, G. Schmidt, C.G. Aneziris, Utilization of recycled material for producing magnesia-carbon refractories, Ceram 6 (2023) 30–42, https://doi.org/10.3390/ceramics6010003.
[23] C. de Repentigny, B. Courcelles, G.J. Zagury, Spent MgO-carbon refractory bricks as a material for permeable reactive barriers to treat a nickel- and cobalt-contaminated groundwater, Environ. Sci. Pollut. Res. 25 (23) (2018) 23205–23214, https://doi.org/10.1007/s11356-018-2414-3.
[24] 5RefrAct, Best Practices in refractory waste management. https://docplayer.net/221939316-Best-practices-in-refractory-waste-management.html.
[25] J.P. Bennet, K.S. Kwong, R. Krabbe, C. Karr, E. Wilson, Spent refractory as slag conditioning additive in the EAF, in: Proceedings of EAF Conference, 2000, pp. 379–390.
[26] S. Strubel, H. Flachberger, R. Nilica, Processing of spent MgO-C refractories: a comparative study between conventional comminution and alternative methods for the liberation of magnesia and carbon, UNITECR (2015) 225. Proceeding.
[27] B.A. Wills, J.A. Finch, Will's Mineral Processing Technology, an Introduction to the Practical Aspects of Ore Treatment and Mineral Recovery, Eight Edition, Butterworth-Heinemann, Oxford, 2016, pp. 102–103.
[28] D. Tromans, Mineral comminution: energy efficiency considerations, Miner. Eng. 21 (2008) 613–620, https://doi.org/10.1016/j.mineng.2007.12.003.
[29] B.P. Numbia, J. Zhanga, X. Xiaa, Optimal energy management for a jaw crushing process in deep mines, Energy 68 (2014) 337–348, https://doi.org/10.1016/j.energy.2014.02.100.
[30] E.G. Kelly, D.J. Spottiswood, Introduction to Mineral Processing, John Wiley & Sons, New York, 1992.
[31] W. Huang, Y. Chen, The application of high voltage pulses in the mineral processing industry – a review, Powder Technol. 393 (2021) 116–130, https://doi.org/10.1016/j.powtec.2021.07.003.
[32] U. Andres, Development and prospects of mineral liberation by electrical pulses, Int. J. Miner. Process. 97 (2010) 31–38, https://doi.org/10.1016/j.minpro.2010.07.004.
[33] P. Zhao, F. Yang, Y. Bai, G. Yan, Z. Sun, H. Zhao, B. Zhang, Analysis and optimization of the selective crushing process based on high voltage pulse energy, Min. Eng. 185 (2022), 107697, https://doi.org/10.1016/j.mineng.2022.107697.
[34] H.-R. Manouchehri, A. Weh, High voltage electric pulse energy in comminuting – case study on Sandvik's Mittersile tungsten ore, Austria, in: XXVIII International Mineral Processing Congress Proceedings, IMPC, 2016, pp. 1–11.
[35] H. Lu, Y. Liu, B. Nie, X. Chen, X. Xu, Crack propagation characteristics of coal samples utilizing high-voltage electrical pulses, ACS Omega 6 (2021) 34395–34405, https://doi.org/10.1021/acsomega.1c04515.
[36] U. Andres, I. Timoshkin, J. Jirestig, H. Stallknecht, Liberation of valuable inclusions in ores and slags by electrical pulses, Powder Technol. 114 (2001) 40–50, https://doi.org/10.1016/S0032-5910(00)00260-6.
[37] K. Bru, S. Touzé, P. Auger, S. Dobrusky, J. Tierrie, D.B. Parvaz, Investigation of lab and pilot scale electric-pulse fragmentation systems for the recycling of ultra-high performance fibre-reinforced concrete, Min. Eng. 128 (2018) 187–194, https://doi.org/10.1016/j.mineng.2018.08.040.
[38] C.L. Duan, Z.J. Diao, Y.M. Zhao, W. Huang, Liberation of valuable materials in waste printed circuit boards by high-voltage electrical pulses, Min. Eng. 70 (2015) 170–177, https://doi.org/10.1016/j.mineng.2014.09.018.
[39] P. Zhao, J. Guo, G. Yan, G. Zhu, X. Zhu, Z. Zhang, B. Zhang, A novel and efficient method for resources recycling in waste photovoltaic panels: high voltage pulse crushing, J. Clean. Prod. 257 (2020), 120442, https://doi.org/10.1016/j.jclepro.2020.120442.
[40] N.P. Mabasa, N. Naudé, A.M. Garbers-Craig, Hand-held XRF sorting of spent refractory bricks to aid recycling, J. S. Afr. Inst. Min. Metall 123 (2023) 9–18, https://doi.org/10.17159/2411-9717/1928/2023.
[41] Astm D4749-87, Standard Test Method for Performing the Sieve Analysis of Coal and Designating Coal Size, ASTM International, West Conshohocken, PA, 2012.